Available online at www.sciencedirect.com
ScienceDirect
Earth and Planetary Science Letters 256 (2007) 61–80
EPSL
www.elsevier.com/locate/epsl

Radioisotopic age constraints for Glacial Terminations IX and VII from aggradational sections of the Tiber River delta in Rome, Italy

Fabio Florindo [a,*], Daniel B. Karner [b], Fabrizio Marra [a], Paul R. Renne [c,d], Andrew P. Roberts [e], Richard Weaver [e]

[a] Istituto Nazionale di Geofisica e Vulcanologia, Via di Vigna Murata, 605, I-00143 Rome, Italy
[b] Department of Geology, Sonoma State University, 1801 East Cotati Avenue, Rohnert Park, CA 94985, USA
[c] Berkeley Geochronology Center, 2455 Ridge Road, Berkeley, CA 94709, USA
[d] Department of Earth and Planetary Sciences, University of California, Berkeley, CA 94720, USA
[e] National Oceanography Centre, Southampton, University of Southampton, European Way, Southampton SO14 3ZH, UK

Received 1 September 2006; received in revised form 8 January 2007; accepted 8 January 2007
Available online 16 January 2007
Editor: M.L. Delaney

Abstract

Buried sedimentary aggradational sections deposited between 800 ka and 600 ka in the Tiber River coastal alluvial plain have been studied using borecores from around Rome. $^{40}Ar/^{39}Ar$ ages on sanidine and/or leucite from intercalated tephra layers and paleomagnetic investigation of clay sections provide geochronologic constraints on the timing of aggradation of two alluvial sections, demonstrating that they were deposited in response to glacio–eustatic sea level rise caused by Glacial Terminations IX and VII. $^{40}Ar/^{39}Ar$ age data indicate ages of 802±8 ka (1σ full errors) and 649±3 ka (1σ full errors) for Glacial Terminations IX and VII, respectively, providing a rare test, beyond the range of U-series dating for corals and speleothems (~500 ka), of the astronomically calibrated timescale developed for oxygen isotope records from deep sea cores.

Keywords: glacial termination; sea level; $^{40}Ar/^{39}Ar$; paleomagnetism; Tiber River delta

1. Introduction

In recent work [1–4], we have shown that glacio–eustatic forcing controlled deposition of sedimentary sections in the alluvial plain of the Tiber River and its tributaries near Rome. Using $^{40}Ar/^{39}Ar$ ages of tephra layers intercalated with the sedimentary deposits and paleomagnetic constraints, we demonstrated that coastal sedimentary sections of the Tiber River and its tributaries were deposited during marine transgressions associated with glacial melting. We have used the geochronology of middle Pleistocene alluvial sections to build an independent chronology of glacio–eustatic cycles for comparison with orbitally-tuned deep-sea $\delta^{18}O$ records.

The sedimentary record of each complete glacially forced sea level oscillation in a coastal area is represented by fluvial incision caused by coastline retreat and lower sea level during glacial periods, and rapid sedimentation in this incised valley caused by sea

* Corresponding author. Tel.: +39 0651860383; fax: +39 0651860397.
E-mail address: florindo@ingv.it (F. Florindo).

0012-821X/$ - see front matter © 2007 Elsevier B.V. All rights reserved.
doi:10.1016/j.epsl.2007.01.014

level rise in response to deglaciation. Here we use the term 'aggradational section' to describe the alluvial sedimentary package left in each incised valley following each glacial maximum. Generally, the aggradational sections that we recognize in Rome are fining-upward sequences, with coarse-grained gravel and sand, approximately 10 m in thickness, at the base of each section. This basal coarse-grained deposit is followed by a thin sand horizon, which grades upward into a several meter thick silt and clay layer. Using $^{40}Ar/^{39}Ar$ ages of intercalated tephra in these aggradational sections, we demonstrated (using sequence stratigraphic terminology) that the coarse-grained deposit formed as part of the lowstand systems tract, whereas the uppermost fine-grained deposits correspond to the transgressive systems tract and early highstand systems tract [1–3].

The area around Rome (Fig. 1) was the site of marine deposition throughout Pliocene and early Pleistocene time. The first appearance of a Tiber River delta, on which a thick succession of clastic sediments accumulated, occurred late in marine isotopic stage (MIS) 22, with deposition of the transgressive sediments of the Monte Ciocci–Monte delle Piche Formation (referred to as the paleo-Tiber 1 unit) (Fig. 2) [4]. Three younger aggradational sections (referred to as the paleo-Tiber 2, 3 and 4 units) (Fig. 2), which were deposited in the time span 800–600 ka, have been identified west of Rome in the Ponte Galeria area, where the Tiber delta prograded into the Tyrrhenian Sea [3]. Ages of tephra layers intercalated in the younger two sections, combined with reversed polarity paleomagnetic data for the oldest aggradational section, allowed Marra et al. [3] to correlate these aggradational sections to MIS 19, 17 and 15 (Fig. 2), respectively.

During the last decade, several attempts have been made to correlate similar alluvial sections in Rome with these coastal sections in the Ponte Galeria area (Fig. 1) [5–8]. However, limited outcrop data, tectonic deformation around Rome, and lack of geochronologic constraints prevented definitive correlation of these sections. We have used data from a large number of wells to reconstruct the underlying stratigraphy. Recently, three 60–80 m rotary cores (hereafter the PSA, VVM and INGV borecores, Fig. 3a, b; see line of section in Fig. 1) were taken by standard rotary drilling techniques by the Istituto Nazionale di Geofisica e Vulcanologia in

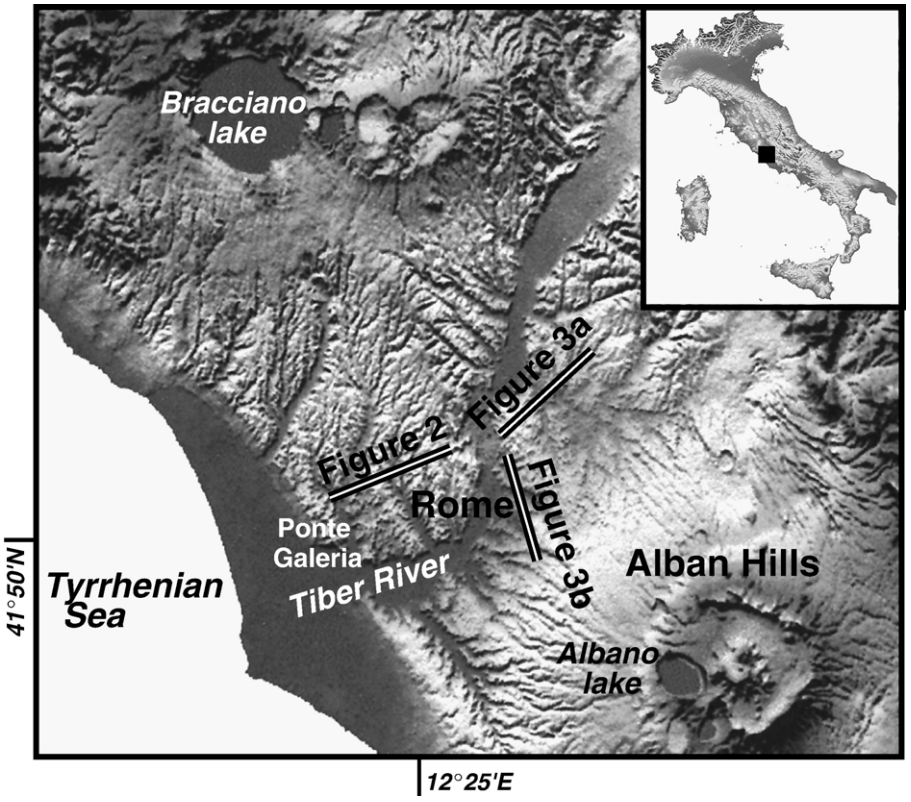

Fig. 1. Digital Elevation Map (DEM) of the Rome area, with lines indicating the position of cross-sections shown in Figs. 2, and 3a b.

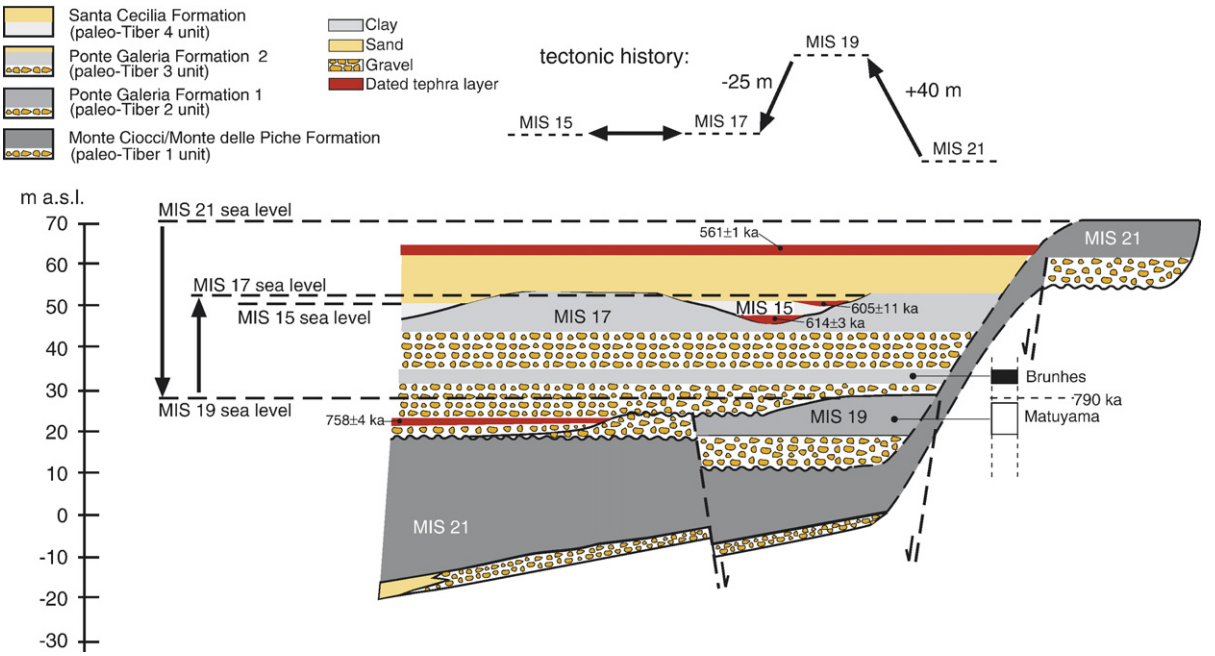

Fig. 2. Cross-section (horizontal not to scale) of the stratigraphy of the paleo-Tiber River sedimentary sections in the Ponte Galeria area west of Rome (see location in Fig. 1). Ages of intercalated tephra layers and paleomagnetically investigated clay sections indicate correlation of these sections to MIS 21 through MIS 15. Past sea level elevations during sea level high stands for each MIS, as inferred from the elevations of highstand systems tracts of the associated sedimentary deposits [3], are also shown. Vertical displacement, which occurred after deposition, is estimated from elevation estimates in Karner et al. [4].

key areas to provide samples for paleomagnetic analysis of clays and $^{40}Ar/^{39}Ar$ age analysis of interbedded tephra horizons. These data refine our larger well log database from the Rome area, which contains approximately 250 well logs.

We present here new $^{40}Ar/^{39}Ar$ and paleomagnetic data from the alluvial sections that were deposited by the Tiber River around Rome between 800 and 600 ka, and we discuss the paleoclimatic implications of the timing of aggradation of these sections. Using these new age constraints, we correlate the sections beneath Rome with those that crop out west of Rome, in the Ponte Galeria area.

2. Stratigraphic setting

Continental sediments around Rome unconformably overlie late Pliocene to early Pleistocene marine clay of the Monte Vaticano Formation [9]. Throughout the area, the oldest aggradational section above the marine substrate is a single 6–8-m-thick gravel layer, which grades upward into sand and clay. An exception to this general stratigraphy occurs in a NW-striking basin (the paleo-Tiber graben; Fig. 3a) NE of Rome, where repeated sections of gravels and clays are above a lowered substrate. The uppermost of these gravel horizons laterally correlates with the single gravel horizon outside the graben.

This oldest aggradational unit is overlain by a several-meter-thick layer of yellow to white sandy clay with abundant carbonate concretions. It is not clear whether this later sedimentary deposit constitutes a new aggradational section correlated to the successive MIS 17, or if it was deposited in the late high stand of MIS 19.

The basal gravel layer of the oldest aggradational unit deepens from north to south: interpretation of borehole stratigraphies (Fig. 3b) suggests that it is fragmented into several blocks that have a horizontal attitude. It was previously interpreted [5] that a single aggradational section of the paleo-Tiber was dislocated by differential vertical movement since its deposition. However, chronostratigraphic investigations in this study identify two different aggradational units, laterally embedded from north to south, which are erosionally above the Plio-Pleistocene substrate in the central-southern area of Rome.

In order to provide radioisotopic age constraints for these aggradational sections, we sampled tephra layers from borecores, and separated potassium-rich mineral phases (sanidine and/or leucite) for $^{40}Ar/^{39}Ar$ age

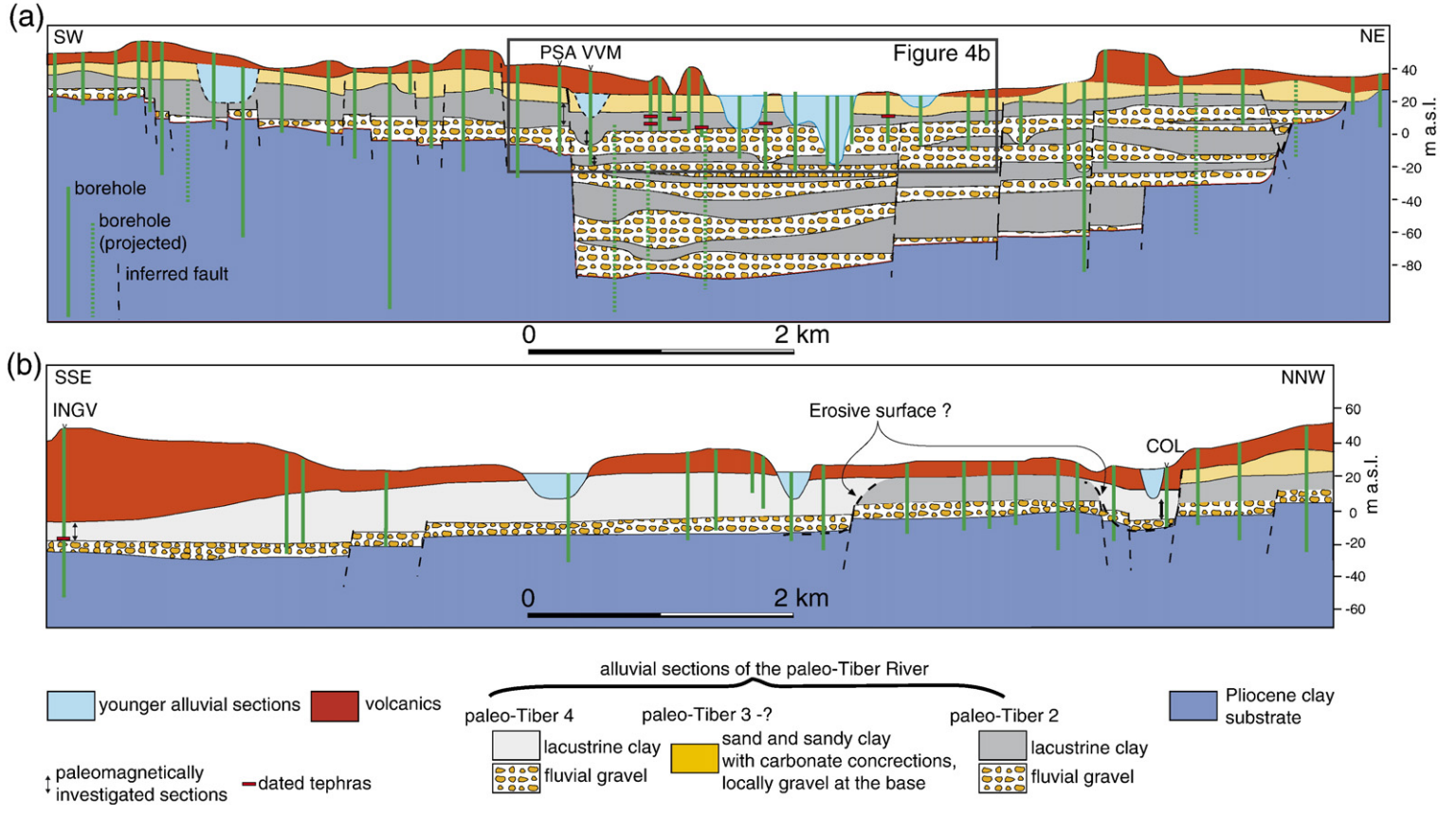

Fig. 3. Cross-sections of the alluvial stratigraphy of the Tiber River around Rome (see location in Fig. 1). Anthropogenic fill is omitted. a) SW–NE oriented cross-section across the paleo-Tiber graben; a single gravel horizon on eroded Pliocene marine substrate is present at the base of the Pleistocene transgressive deposits in the southwest, whereas repeated successions of gravel and clay fill the graben to the northeast. The clay horizon above the gravel has reversed geomagnetic polarity, which indicates that deposition preceded the Matuyama/Brunhes geomagnetic reversal (see text) (780 ka, [10]). b) SSE–NNW oriented cross-section through central-southern Rome. A single gravel horizon is present in this area. The clay horizon above the gravel has normal geomagnetic polarity, which indicates deposition during the Brunhes Chron (see text). Ages of intercalated tephra layers also confirm younger deposition for the clay in southern Rome. The erosional surface separating the two sedimentary sections is tentatively drawn in b) based on stratigraphic and paleogeographic (see text) evidence. The detailed stratigraphy within the grey box is shown in Fig. 4b.

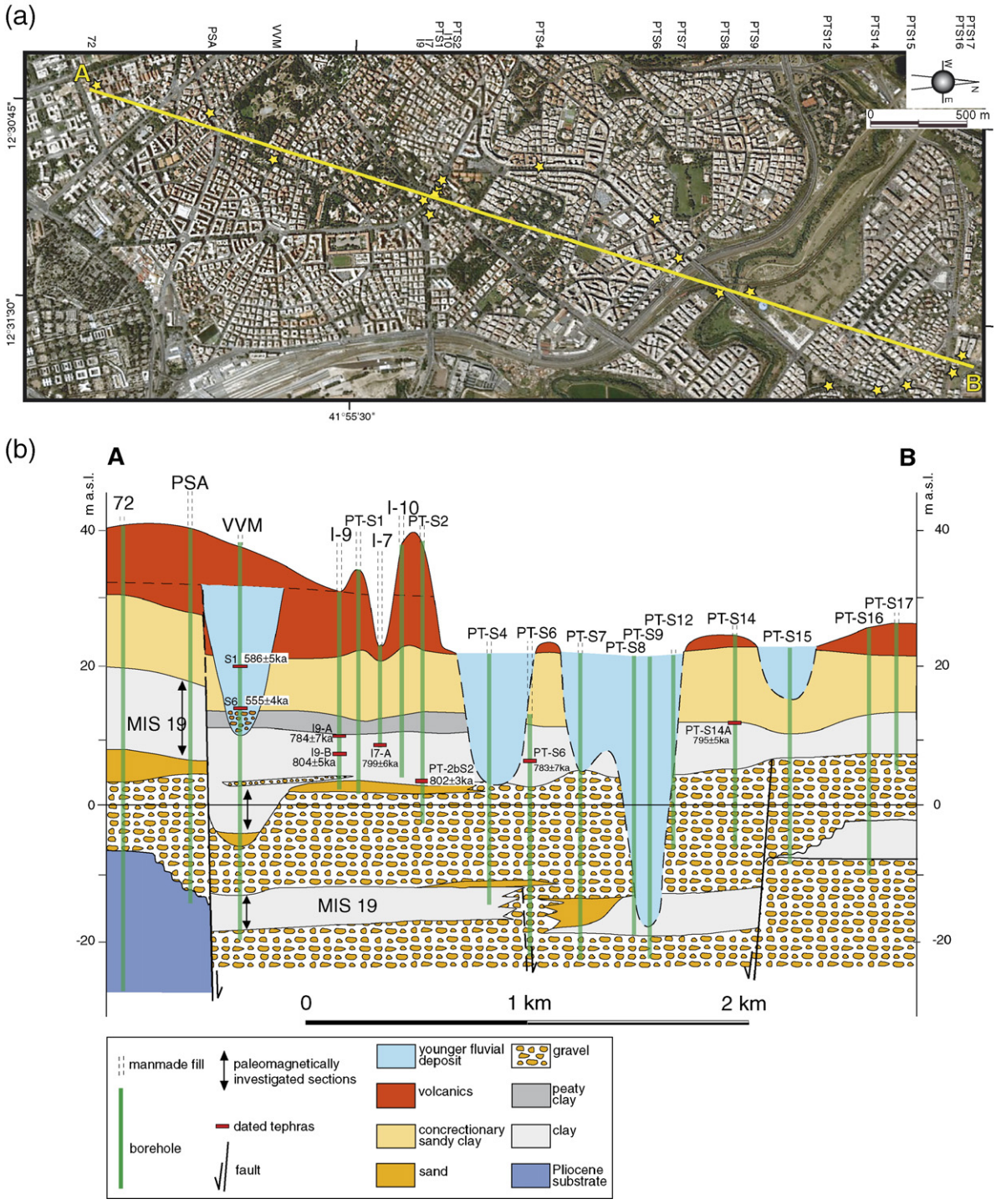

Fig. 4. a) Location of the drilled sites. b) Enlarged portion of the cross-section of Fig. 3a, with details of the sedimentary sections studied from borecores and sampled for paleomagnetic and radioisotopic age analyses. On the left side, PSA and VVM are the borecores drilled for this study.

analysis. In addition, clayey intervals, when suitable, were sampled for paleomagnetic investigation. The occurrence of the Matuyama–Brunhes (M–B) geomagnetic reversal (780 ka, [10]) offers us the opportunity to use paleomagnetic data to distinguish clay sections deposited during MIS 19 from thos of MIS 17.

Relatively few tephra layers exist in these sedimentary sections because the major explosive activity in the volcanic districts of this region started after 600 ka [11]. However, six tephra layers were recovered in five borecores (PT-S2, I-9, I-7, PT-S6, PT-S14; see Fig. 4) drilled in the paleo-Tiber graben. All of these tephra layers occur in the uppermost clay horizon. Two of these tephra (from borecores PT-S2, PT-S6) were dated by Karner et al. [11] and yielded ages of 802 ± 3 ka and 783 ± 7 ka, respectively, based on the age of 28.02 Ma for the irradiation standard Fish Canyon Tuff sanidine [12].

Another tephra layer was recovered in southern Rome from the INGV borecore (Fig. 3b). Here, a single gravel horizon is present, unconformably overlying a Pliocene marine clay substrate. On top of this gravel, a 1-m-thick pyroclastic-flow deposit was recovered. Above it, a sandy deposit grades upward into lacustrine clay. A well-developed, oxidized soil on top of the lacustrine clay separates it from the overlying volcanic succession. A pumice fall deposit at the base of the volcanic succession has an $^{40}Ar/^{39}Ar$ age of 582 ± 1 ka [11] based on the age of 28.02 Ma for Fish Canyon Tuff sanidine, whereas deeper in the section, two samples from the pyroclastic-flow deposit within the sedimentary section were dated [11] at 649 ± 4 ka and 656 ± 2 ka, respectively, also based on Fish Canyon Tuff sanidine. Based on the different radioisotopic ages for the tephra layers dated from the northern (PT-S2, I-9, I-7, PT-S6, PT-S14 borecores; Fig. 4) and southern (INGV borecore) areas, it is apparent that the aggradational sections in the two sectors (Fig. 3) must correlate to different glacio–eustatic sea level rises, namely to MIS 19 and MIS 15, respectively.

In order to constrain further the correlation with marine isotopic stages and to resolve conflicts with previous chronostratigraphic interpretations [5,6], we drilled two new boreholes and sampled other cores for $^{40}Ar/^{39}Ar$ age analysis of tephra layers and paleomagnetic assessment of clay horizons. These included cores from the transition zone between the area where the multi-layered gravel succession is present and the area where a single gravel horizon occurs at the base of the aggradational section beneath Rome. In addition, we paleomagnetically investigated the clay section deposited above the pyroclastic flow deposit dated at around 650 ka in the INGV borecore.

Despite our investigation of many borecores drilled between the center of Rome and the INGV borecore site, no tephra layers have been identified within sediments from this area. All the recovered tephra layers are from sedimentary successions in tectonically lowered sectors of Rome. This suggests that rapid burial during syn-sedimentary subsidence preserved these thin tephra horizons, whereas in other areas they were removed or reworked by fluvial erosion.

3. Methods

3.1. $^{40}Ar/^{39}Ar$ geochronology

Volcanic material was sampled from six sediment cores. The tephra layer from the INGV borecore is a massive, zeolitized, ash matrix-supported deposit, including mm-to cm-sized yellow and grey scoria clasts, yellow pumice clasts, lava and tuff lithic clasts, and mm-sized leucite and sanidine crystals. Petrochemical characteristics of this deposit are the same as those of several other primary pyroclastic flow deposits erupted from the Monti Sabatini Volcanic District that crop out throughout Rome [11]. The material sampled in the five borecores to the north of Rome included graded and well-stratified ash-fall deposits (samples PT2B-S2, PTS6-A, I9-B), which are interpreted to be primary, massive tuffaceous horizons that indicated a sudden flux of volcanic material into the Tiber River (samples I9-A, PT-S14), and highly concentrated volcaniclastic sediment (samples I7-A, VVM-S1, VVM-S2).

While the age data acquired for each of these materials can be straightforward to interpret, these data must be carefully applied to the chronostratigraphic history of the Tiber River system to account for (possibly) significant delays between eruption and deposition in the sedimentary system. While deposition of primary ash falls is nearly instantaneous, the delay could be significant for reworked volcaniclastic horizons. For those horizons, we rely on other data (e.g., stratigraphic consistency with other well-dated key horizons) to support our age interpretations, but several samples can only be used to provide minimum age constraints.

$^{40}Ar/^{39}Ar$ analyses were conducted at the Berkeley Geochronology Center using facilities and procedures similar to those described by Karner and Renne [1]. When possible, sanidine and leucite phenocrysts were used for independent age analysis, but for some samples, only one mineral phase was present. Mineral separates were cleaned in an ultrasonic bath of 7% HF for approximately 60 s to remove adhered glass and to reduce surficial atmospheric argon contamination. Leucite and sanidine mineral separates were placed in aluminum disks along with the Alder Creek Tuff sanidine standard or the Fish Canyon Tuff sanidine standard (1.194 Ma and 28.02 Ma, respectively, Renne et al. [12]) and irradiated in the CLICIT facility at the Oregon State University TRIGA reactor for approximately 30 minutes, where cadmium shielding is employed to

minimize the $^{40}K(n,p)^{40}Ar$ reaction caused by thermal neutrons [13].

Two fully automated microextraction-mass spectrometer systems were used for the $^{40}Ar/^{39}Ar$ analyses, as described by Karner and Renne [1]. The MAP1 system includes a 6 W continuous Ar-ion laser for sample heating, and a Mass Analyzer Products (MAP) 215 90° sector extended-geometry mass spectrometer for isotopic analysis. MAP-III includes a CO_2 laser and a MAP 215-50 90° sector extended-geometry mass spectrometer with electrostatic analyzer. Background corrections were made from full system blanks, which were run between every three unknowns. Released gases were scrubbed of reactive species using Zr–Fe–V and Zr–Al alloy getters, and the remaining gases were then admitted into the mass spectrometer, where the Ar ion beam currents were measured on an electron multiplier. Mass discriminations (1.006–1.010/amu for MAP1, 1.007/amu for MAPIII), applied as a power law correction, were determined by analysis of atmospheric argon from air pipettes. Argon isotopes were corrected using procedural blanks; long-term blank values were regressed such that between-blank variance was propagated as a component of uncertainty.

Single-crystal total fusion analyses were performed on each sample whenever possible. However, some of the samples contained crystals that were too small to yield high-precision single-crystal ages. In these cases, multiple-crystal total-fusion analyses were made. Additional analyses were made on samples suspected of having xenocrystic contamination, in order to improve the chance of resolving the youngest age population. Ages (Table 1) are calculated from the error-weighted mean $^{40}Ar/^{39}Ar$ ratios [14]. The best age estimate for each sample is the error-weighted mean age from the youngest statistically-consistent population of crystals, whereby the individual measurements were required to be within 2σ of the error-weighted mean value for inclusion in the best age calculation. This criterion was used to identify and eliminate xenocrysts or alteration from the best age estimate. Ages are reported with 1σ analytical precision in Table 1. We also report for the best ages the full errors that take into account the systematic age errors inherent to the $^{40}Ar/^{39}Ar$ method (see [1]). The inclusion of systematic errors is necessary for accurate comparison with the orbital chronologies used to date glacial cycles, and hence is important for the paleoclimate interpretations made later in this paper. Some age data that we reported previously [11] were reprocessed here, to assess whether they are from the same population, or distinct populations, as those samples analyzed here. To make this comparison in an unbiased way, we reprocessed those data from Karner et al. [11] using the same data reduction method used for the new data. These ages therefore differ slightly from what we have reported in our earlier publications, but are well within previously stated analytical precisions.

Table 1
$^{40}Ar/^{39}Ar$ dates for ashes from the paleo-Tiber sequences

Analyses in final							
Lab. No.	Sample	Mineral	age/total analyses	Age (ka)	$\pm1\sigma$ [a]	$\pm1\sigma$ [b]	MSWD [c]
33169	VVM-S6	Leucite	2/7	554.1	3.7	6.4	0.3
33170	VVM-S6	Sanidine	5/7	554.9	3.7	6.4	0.8
	VVM-S6 (best)	s+1	7/14	554.5	3.5	6.3	0.6
33176	VVM-S1	Sanidine	4/5	585.9	4.7	7.3	3.4
10804	ING-02	Sanidine	3/4	583.0	1.8	5.7	1.7
10805	ING-02	Leucite	7/8	582.1	1.5	5.6	2.3
	ING-02 (best)	s+1	10/12	582.4	1.4	5.6	1.9
10800	ING01-P1	Sanidine	5/22	648.8	3.8	7.1	2.4
10801	ING01-P1	Leucite	1/6	649.9	2.6	6.5	N.A.
	ING01 (best)	s+1	6/28	649.3	1.9	3.4	0.3
11083	PTS6-A	Sanidine	13/13	783.1	6.6	9.8	0.4
33180	I9-B	Sanidine	7/8	793.6	7.9	11.0	0.1
33179	I9-B	Leucite	7/7	804.6	5.2	9.3	1.3
	I9-B (best)	s+1	14/15	803.7	5.2	9.2	0.9
33182	I9-A	Sanidine	7/8	783.7	6.7	10.0	0.2
33181	I7-A	Sanidine	5/6	799.3	6.2	9.8	0.2
33178	PTS14-A	Sanidine	7/8	795.2	5.4	9.3	1.5
10813	PT2B-S2	Sanidine	6/8	802.4	2.9	7.9	1.5

[a] Analytical precision.
[b] Includes systematic error inherent to the 40Ar/39Ar method (see Karner and Renne [1]).
[c] MSWD=Mean square weighted deviation=$\chi^2/N-1$.

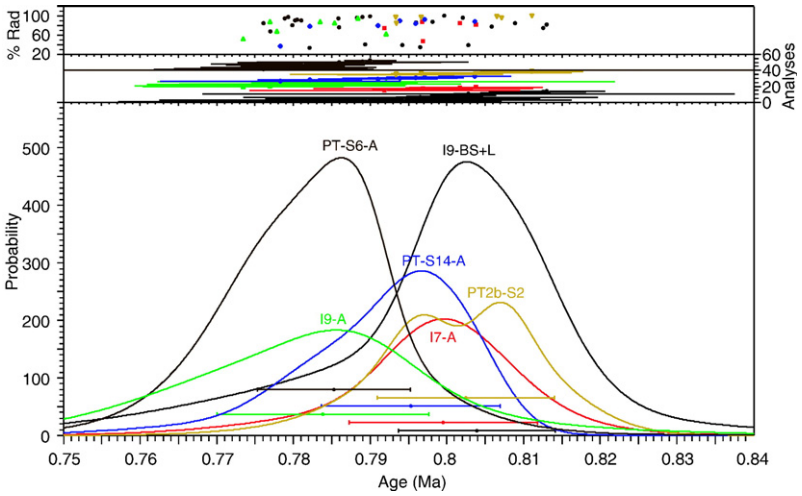

Fig. 5. Ideograms (age probability diagrams, using 2σ error distributions) of the six samples recovered from borecores in the sediment of the paleo-Tiber River north of Rome. The existence of two tephra layers within the same core (I9-A and I9-B) indicates that at least two eruptive events occurred.

3.2. Paleomagnetism

Two clay sections to the north and to the south of Rome, for which radioisotopic age data indicated ages respectively older and younger than the Matuyama–Brunhes reversal, have been paleomagnetically investigated. Consolidated fine-grained horizons in the VVM, PSA (northern sector) and INGV (southern sector) borecores were sampled by drilling conventional cylindrical paleomagnetic samples (25 mm diameter × 22 mm height) using a gasoline-powered hand drill with a water-cooled diamond bit. Fifty-one oriented discrete samples were collected from the VVM (19 samples), PSA (12 samples) and INGV borecores (20 samples). The borecores were not azimuthally oriented. All samples were oriented with respect to vertical to enable polarity determinations on the basis of paleomagnetic inclinations.

The natural remanent magnetization (NRM) was analysed within the magnetically shielded paleomagnetic laboratory at the Istituto Nazionale di Geofisica e Vulcanologia, Rome, using a 2-G Enterprises (model 755) narrow-access pass-through cryogenic magnetometer, equipped with in-line alternating field (AF) demagnetization capability. The NRM was stepwise AF demagnetized at successive peak fields of 5, 10, 15, 20, 25, 30, 40, 50, 60, 70, 80, 90 and 100 mT. Samples from the VVM and INGV cores were also thermally demagnetized at steps of 30–40 °C from room temperature until the remanences became unstable. Demagnetization data were examined using orthogonal vector component diagrams, stereographic projections and intensity decay curves. Characteristic remanent magnetization (ChRM) components were determined from principal component analysis using data from multiple demagnetization steps [15]. The maximum angular deviation (MAD) was calculated to provide an estimate of the precision related to each best-fit line. Data with MAD $\geq 10°$ were considered poorly defined and are not presented here. Mineral magnetic analyses, based on magnetic coercivity and thermal unblocking characteristics, were conducted on a set of representative discrete samples.

Sediment microtextures were investigated using 12 polished thin sections in order to examine the magnetic mineralogy. A LEO 1450VP scanning electron microscope (SEM), operated at 15 keV at the National Oceanography Centre, Southampton, was used for these observations. Elemental analyses were obtained from energy-dispersive X-ray spectra generated from point analyses (2–3 μm beam diameter) of individual mineral grains, or of clusters of grains, using a Princeton Gamma Tech (IMIX-PTS) system.

4. Results

4.1. $^{40}Ar/^{39}Ar$ geochronology

4.1.1. Northern sector

$^{40}Ar/^{39}Ar$ ages are reported in Table 1. Only one (I9) of the five borecores that contained clay deposits from the northern sector of the Tiber River contained two tephra layers (Fig. 4), which enables us to distinguish at least two eruptive events from the series of samples

whose ages are statistically indistinguishable (Fig. 5). Visual inspection of these two deposits suggests that both are primary deposits with significantly different petrographic characteristics.

Sample I9-B, the stratigraphically lower deposit, is a yellow ash with approximately 10% by volume red to brown scoria lapilli. The deposit contains a basal horizon of grain-supported ash consisting of yellow pumice, scoria, and crystals of leucite, sanidine, clinopyroxene, and rare biotite. The deposit grades upward into a matrix-supported ash. The overall textural and stratigraphic features of this layer indicate that it is a primary ash fall horizon. The combined $^{40}Ar/^{39}Ar$ age from both the leucite and sanidine crystal populations is 804±5 ka.

Sample I9-A, which lies above I9-B, consists of fine-grained yellow ash with a minor white to yellow pumice lapilli component. Sanidine is common, while clinopyroxene, biotite and leucite are rare. Compared to sample

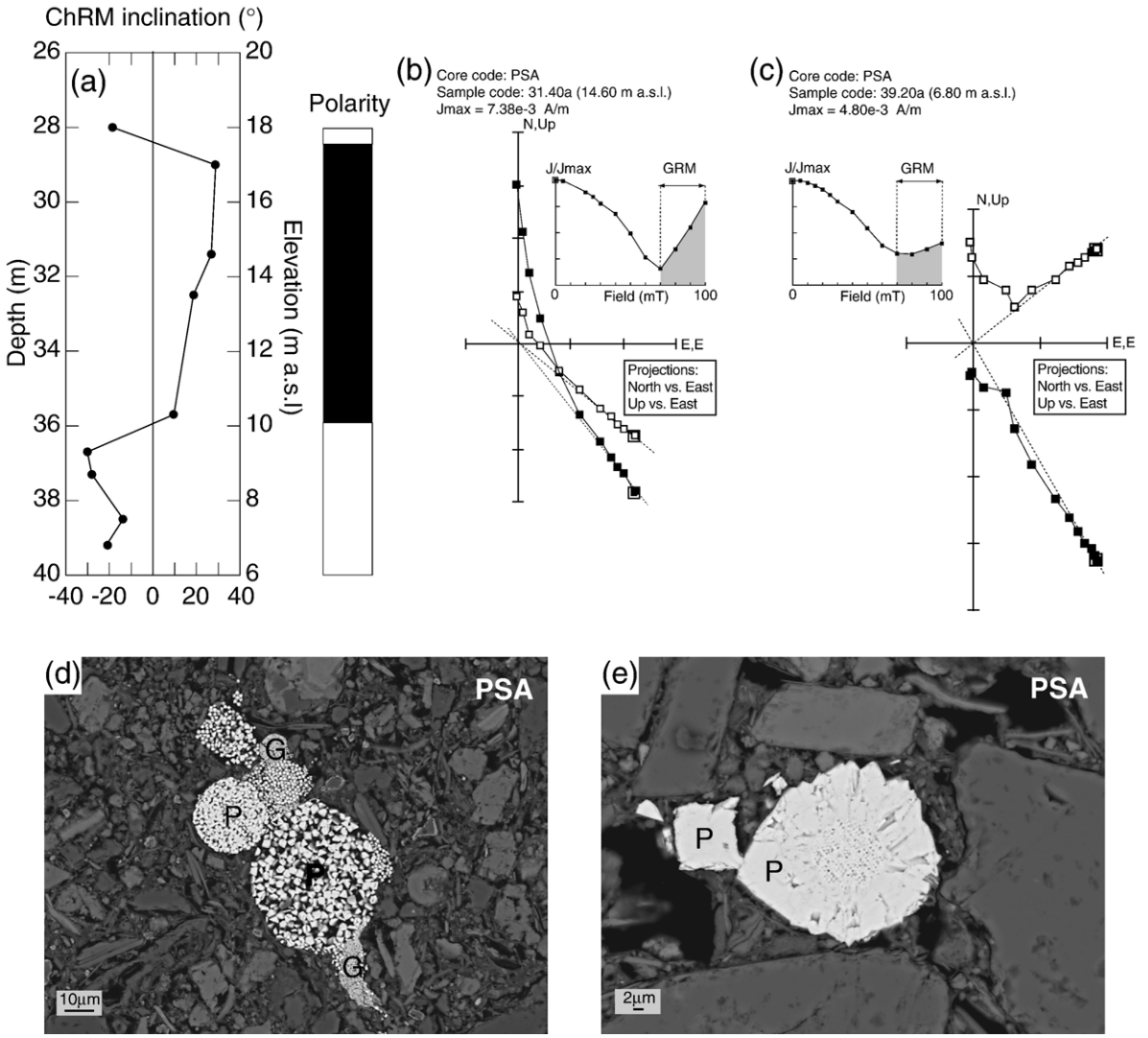

Fig. 6. Core PSA. (a) Stratigraphic plot of the ChRM inclination, and polarity zonation. (b, c) AF demagnetization plots for two samples from a depth of 31.40 (normal polarity) and 39.20 m (reverse polarity), respectively. The AF demagnetization data indicate acquisition of a GRM at fields above 60 mT. For the vector component diagram, open (closed) symbols represent projections onto the vertical (horizontal) plane. Samples are not azimuthally oriented and declinations are reported in the laboratory coordinate systems. (e, f) Representative back-scattered electron images of iron sulphide minerals from polished sections. (e) Pyrite (P) framboids with circular cross-section, composed of relatively large individual crystals, surrounded by less regularly shaped patches of finer-grained greigite (G) crystals (sample from 37.3 m in core PSA). (f) Early diagenetic pyrite framboid (center) that has been overgrown/recrystallized by later euhedral pyrite (sample from 39.2 m in core PSA).

I9-B, sample I9-A is not obviously graded, it has fewer crystals, and does not contain scoria lapilli. Given the differences between this unit and I9-B, we interpret I9-A to be from a distinct volcanic eruption, and that it probably was a pumice and ash fall. Sanidine from sample I9-A yielded an $^{40}Ar/^{39}Ar$ age of 784±7 ka.

Two additional tephra samples intercalated at different depths in the same clay horizon from the northern sector of the Tiber River clay deposits were previously collected [12] from two different borecores (PT-S2 and PT-S6, Fig. 4). The ages of these two tephra are recalculated here to be 802±3 ka (lower), and 783±7 ka (upper), respectively, which agree well with the ages obtained for samples I9-B and I-9A. Finally, two samples from two other borecores (I-7 and PT-S14; Fig. 4) yielded ages of 799±6 ka and 795±5 ka, respectively. These ages are indistinguishable (including systematic errors) from either the older or the younger ages from borecore I-9, and do not provide any further constraint.

The number and ages of distinct eruptive events can be assessed by considering stratigraphic evidence for two eruptions in borecore I-9, with their associated radioisotopic ages of 804±5 ka and 784±7 ka, along with ages from samples PT-2bS2 and PTS6-A (802±3 ka, 783±7 ka) which display clear features of a primary deposit. Combining the ages of these two groups of samples yields ages of 803±8 ka and 783±10 ka (1σ, including systematic errors) for the two eruptive events. Two samples of highly concentrated volcaniclastic material were also collected from an aggradational section that lies unconformably above the older paleo-Tiber clay deposit in borecore VVM (Fig. 4). From bottom to top, these samples (VVM-S6 and VVM-S1, Fig. 4) yielded stratigraphically inconsistent ages of 554±4 and 586±5 ka, indicating reworking.

4.1.2. Southern sector

We re-calculated the ages of two samples from core INGV (Fig. 3b) consisting of a massive yellow ash containing infrequent scoria lapilli, and a phenocryst assemblage that is dominated by sanidine and black to green clinopyroxene [11]. Small, rounded sedimentary clasts also occur in this sample, which indicate that some reworking of the underlying gravel layer occurred during emplacement, as is expected in a pyroclastic flow deposit. Out of 34 separate age analyses, 27 of which were on single crystals and 7 of which included two crystals, only six single crystal analyses were included in the best age estimate. The error-weighted mean age for these six analyses is 649±2 ka (1σ). By including the systematic errors, the age is 649±3 ka (1σ).

4.2. Paleomagnetism

4.2.1. Northern sector — PSA borecore

The magnetization of the sampled clay interval in the PSA core is complex and is characterized by acquisition of gyroremanent magnetizations (GRMs) during AF demagnetization at peak fields greater than 50–60 mT (Fig. 6). This behaviour is related to the ubiquitous presence of magnetic iron sulphide minerals (Fig. 6 d, e), but, despite the fact that the demagnetization behaviour is far from ideal, it is still possible to isolate a ChRM at peak fields ≤50–60 s mT. Samples from the lowermost portion of the PSA core (below ca 10.0 m a.s.l.) have a clear reversed polarity magnetization (Fig. 6a, b), which indicates that this portion of the core is older than the M–B boundary, in agreement with the $^{40}Ar/^{39}Ar$ ages obtained in the nearby borecores where tephra layers intercalated in the clay have been dated at 804±5 and 783±7 ka (Fig. 4b). The dominance of normal polarity between 10 and 17.58 m a.s.l (Fig. 6a) is probably indicative of remagnetization during the Brunhes Chron (see discussion below).

4.2.2. Northern section— VVM borecore

The sampled clay intervals in borecore VVM have consistently stable magnetizations, as indicated by both AF and thermal demagnetization results (Fig. 7a–c). This permits development of a clear polarity sequence. A reversal boundary is recorded in the VVM core at 14.2 m a.s.l. $^{40}Ar/^{39}Ar$ ages (Fig. 4b) suggest that this magnetic reversal occurs too low in the sequence to mark the position of the M–B boundary. While the clay section that lies above the gravel layer in borecore PSA has reversed polarity in the lower part of the studied interval, the same clay section in the VVM borecore has a normal polarity magnetization. We therefore conducted detailed mineralogical investigations to verify whether the apparent mismatch between the $^{40}Ar/^{39}Ar$ ages and the variable position of the observed reversed to normal polarity transition (which might otherwise have been interpreted to indicate the M–B boundary) can be explained by a late diagenetic remagnetization.

Thermal demagnetization of the studied samples indicates a major unblocking at 300–400 °C (Fig. 7b), which is consistent with the presence of greigite (Fe_3S_4) (e.g. [16]) or monoclinic pyrrhotite (Fe_7S_8) (e.g. [17]). AF demagnetization of replicate samples from the same stratigraphic horizons results in acquisition of a GRM at peak fields above 50–60 mT, parallel to the last axis along which an AF was applied (Fig. 7c). GRM acquisition is common in single domain (SD) magnetic grains, particularly in magnetic iron sulphides such as

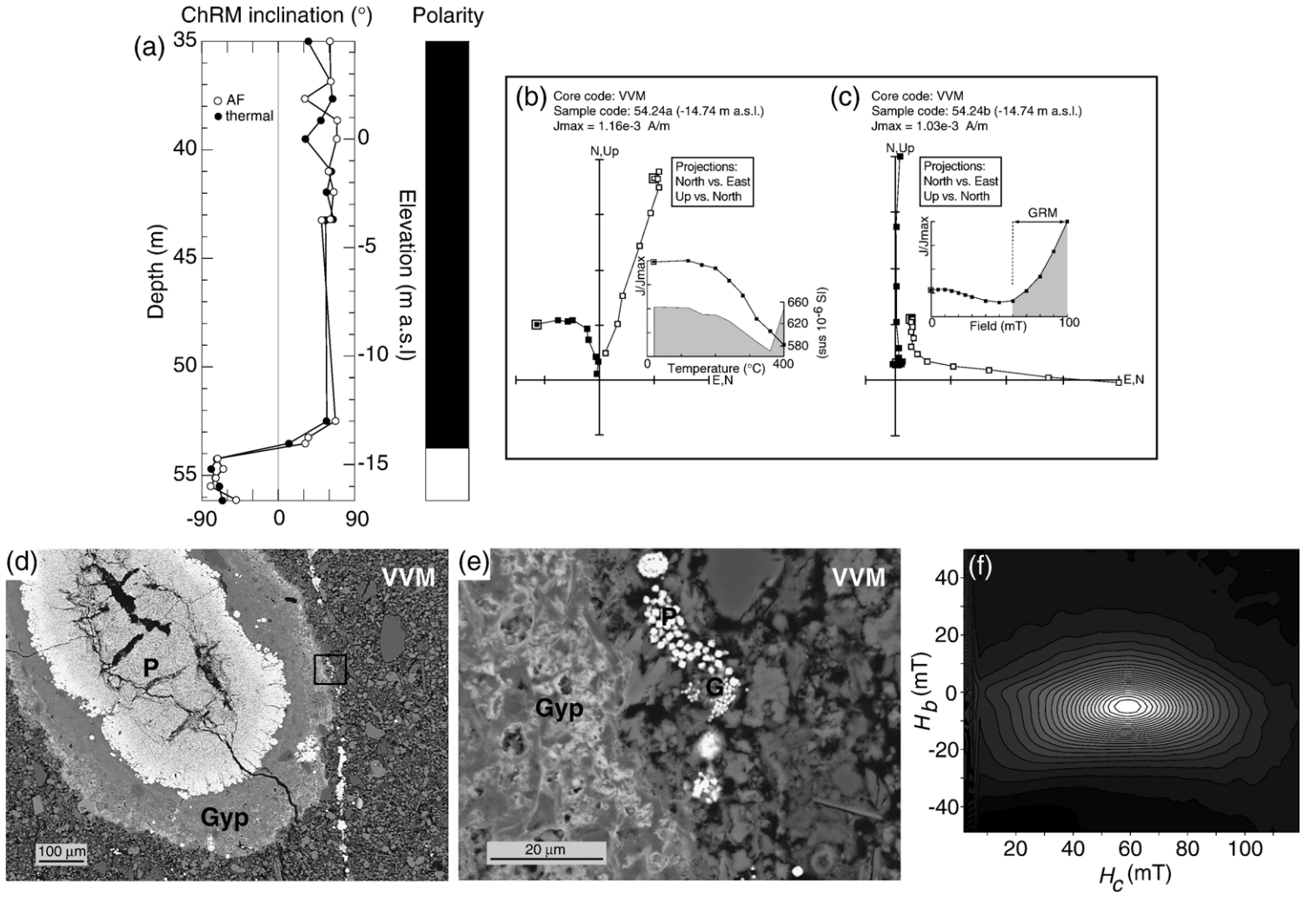

Fig. 7. Core VVM. (a) Stratigraphic plot of the ChRM inclination, and polarity zonation. Representative (b) thermal and (c) AF demagnetization data for replicate samples from a depth of 54.24 m. The AF demagnetization data indicate acquisition of a GRM at fields above 60 mT and the thermal demagnetization data indicate a major decay in remanence intensity at 200–400 °C, both of which are indicative of a magnetic iron sulphide mineral. For the vector component diagram, open (closed) symbols represent projections onto the vertical (horizontal) plane. Samples are not azimuthally oriented and declinations are reported in the laboratory coordinate systems. (d, e) Representative back-scattered electron images of iron sulphide minerals from polished sections. (d) A pyrite nodule from a sample from 43.20 m, the surface of which has been oxidized to form gypsum (Gyp). Later-formed pyrite and greigite are present around the edges of the gypsum (box shows area of high-magnification image in (e)). (e) High-magnification view of pyrite and greigite that has grown on the surface of gypsum that formed via oxidation of the pyrite nodule shown in (d). (f) Representative FORC diagram (smoothing factor, SF = 4) for a sample from 32.50 m in core PSA, which indicates the presence of a relatively high coercivity mineral ($H_c = \sim 55$ mT) with significant magnetostatic interactions, both of which are typical of magnetic iron sulphide minerals (cf. Roberts et al. [20,21]).

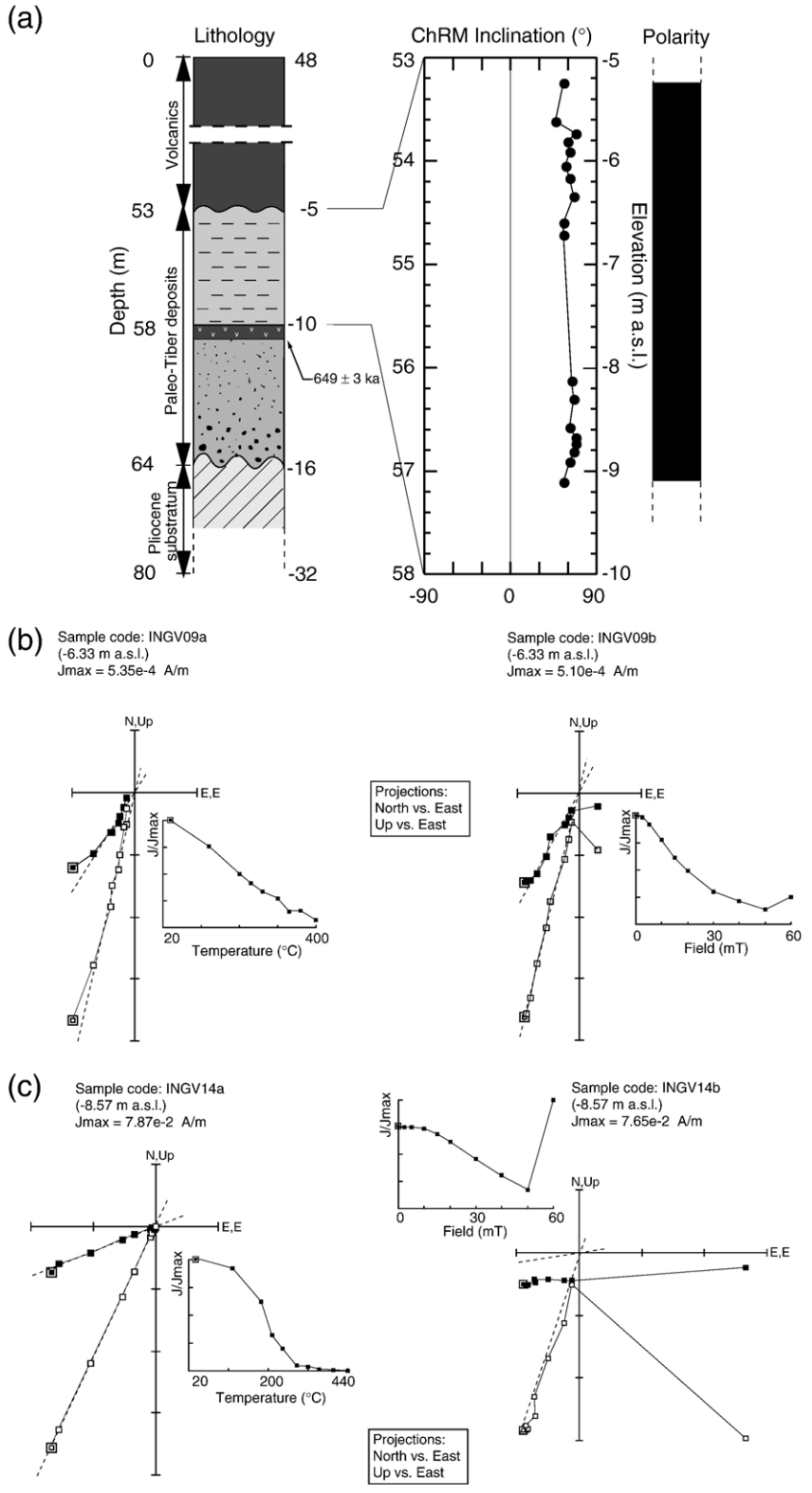
(a)
Lithology
ChRM Inclination (°)
Polarity
Depth (m)
Elevation (m a.s.l.)
Volcanics
Paleo-Tiber deposits
Pliocene substratum
649 ± 3 ka
(b)
Sample code: INGV09a
(-6.33 m a.s.l.)
Jmax = 5.35e-4 A/m
Sample code: INGV09b
(-6.33 m a.s.l.)
Jmax = 5.10e-4 A/m
N,Up
E,E
J/Jmax
Temperature (°C)
Field (mT)
Projections:
North vs. East
Up vs. East
(c)
Sample code: INGV14a
(-8.57 m a.s.l.)
Jmax = 7.87e-2 A/m
Sample code: INGV14b
(-8.57 m a.s.l.)
Jmax = 7.65e-2 A/m

greigite (e.g. [18,19], for which SD-like behaviour is commonly documented [16]. Confirmation of the SD nature of the magnetic iron sulphide grains is provided by a typical first-order reversal curve (FORC) diagram for these sediments (Fig. 7f), which is similar to those for other greigite-bearing sediments [20,21]. Finally, we have unequivocally demonstrated the presence of greigite by back-scattered electron imaging (e.g., Fig. 7d, e). The sediments contain patches of iron sulphide aggregates that include spherical (circular in cross-section) pyrite framboids made up of reasonably large (~1 μm) pyrite octahedra. Many of these patches of iron sulphides also contain less regularly shaped aggregates of much finer-grained greigite crystals. These greigite grains appear to be responsible for the magnetization of the studied sediments and the close packing of the grains is responsible for the substantial magnetostatic interactions evident in the vertical spread of the FORC distribution (Fig. 7f). All samples subjected to paleomagnetic analysis provide evidence for a magnetic iron sulphide (e.g., Fig. 6b, c) and all of the polished sections investigated using the SEM contain greigite. No other magnetic iron sulphides were documented.

In most cases, greigite occurs in aggregates of the type shown in Fig. 6d. Such occurrences give little clear microtextural evidence about the timing of greigite formation (except that it grew after the nearby pyrite framboids). Overgrowth of euhedral pyrite on early diagenetic pyrite framboids is common in these samples (e.g., Fig. 6e), which indicates prolonged exposure to pore water sulphide with evolution of pore waters over time [22]. Some samples provide more direct evidence that these sediments were remagnetized. In these cases, pyrite nodules with dimensions of 0.5–1 mm are observed (e.g., Fig. 7d). The centers of these nodules are made up of microcrystalline pyrite, which is surrounded and overgrown by amorphous gypsum ($CaSO_4.H_2O$) (Fig. 7d). It is not clear whether these nodules grew during early diagenesis or during later sulphidization. Variable corrosion of the edges of the pyrite nodule in Fig. 7d, and the halo around this nodule, indicate a fluid-rock interaction and suggest that the gypsum grew as a result of reactions involving the underlying pyrite. Iron sulphides, which are evident as bright regions with high electron backscatter, appear to have grown even later on the outer edges of the gypsum (Fig. 7d). A close-up view of the boxed area in Fig. 7d is shown in Fig. 7e, which demonstrates that these later-formed sulphides include coarser-grained pyrite and finer-grained greigite. Microtextural evidence for the growth of this greigite after gypsum provides evidence for a later diagenetic growth (i.e. not syn-depositional early diagenetic growth) that can explain the observed remagnetization (see [23] for more details).

In the Tiber River sediments, gypsum only occurs in association with pyrite nodules and the sulphate in the gypsum appears to have been derived from the sulphide in the pyrite. For this sulphate to sulphide reaction to occur, pyrite must undergo oxidation (see [23] for details). The Tiber River clays were deposited in a brackish environment [5] under anoxic conditions that were suitable for pyrite formation. These sediments are likely to have undergone oxidation by percolation of oxic pore waters during deposition of the intercalated gravels. Oxidation of pyrite nodules is therefore likely to have occurred during periods of lowered sea level. A later return to anoxic conditions during a later marine transgression would have given rise to conditions where sulphate in the gypsum could react with available iron to form late diagenetic greigite and pyrite, as observed in Fig. 7e (the relevant chemical reactions and mineralogical transformations are given by [23]). The later diagenetic formation of greigite in these sediments appears to be a direct result of non-steady state diagenesis that was driven by major changes in pore water conditions associated with large amplitude sea level changes. Late diagenetic remagnetizations involving greigite are being increasingly documented (e.g. [23–27]), which suggests that greigite can be a paleomagnetically problematical mineral. Overall, our SEM observations provide a solution to the apparent contradiction between high precision $^{40}Ar/^{39}Ar$ ages and paleomagnetic determinations because they confirm that the clays have been remagnetized as a result of late diagenetic greigite growth. In this case, the $^{40}Ar/^{39}Ar$ ages provide a more robust indication of the depositional age of the Tiber River sediments.

4.2.3. Southern sector — INGV borecore

All of the collected paleomagnetic samples from the clayey interval of the INGV borecore (from 48.0 to −32 m a.s.l.; Fig. 3) are characterized by a stable and well defined normal polarity magnetization (Fig. 8).

Fig. 8. Core INGV. (a) Lithology, stratigraphic plot of the ChRM inclination, and polarity zonation. (b) Representative thermal and AF demagnetization data for replicate samples from −6.33 m a.s.l. (c) Representative thermal and AF demagnetization data for replicate samples from −8.57 m a.s.l. For the vector component diagram, open (closed) symbols represent projections onto the vertical (horizontal) plane. Samples are not azimuthally oriented and declinations are reported in the laboratory coordinate systems.

Further demagnetization above 400 °C results in random paleomagnetic directions. By analogy to the demagnetization results from the PSA and VVM cores (Figs. 6 and 7) the demagnetization data for the INGV borecore are consistent with the presence of greigite. Rock magnetic analyses (not shown here) for the lower

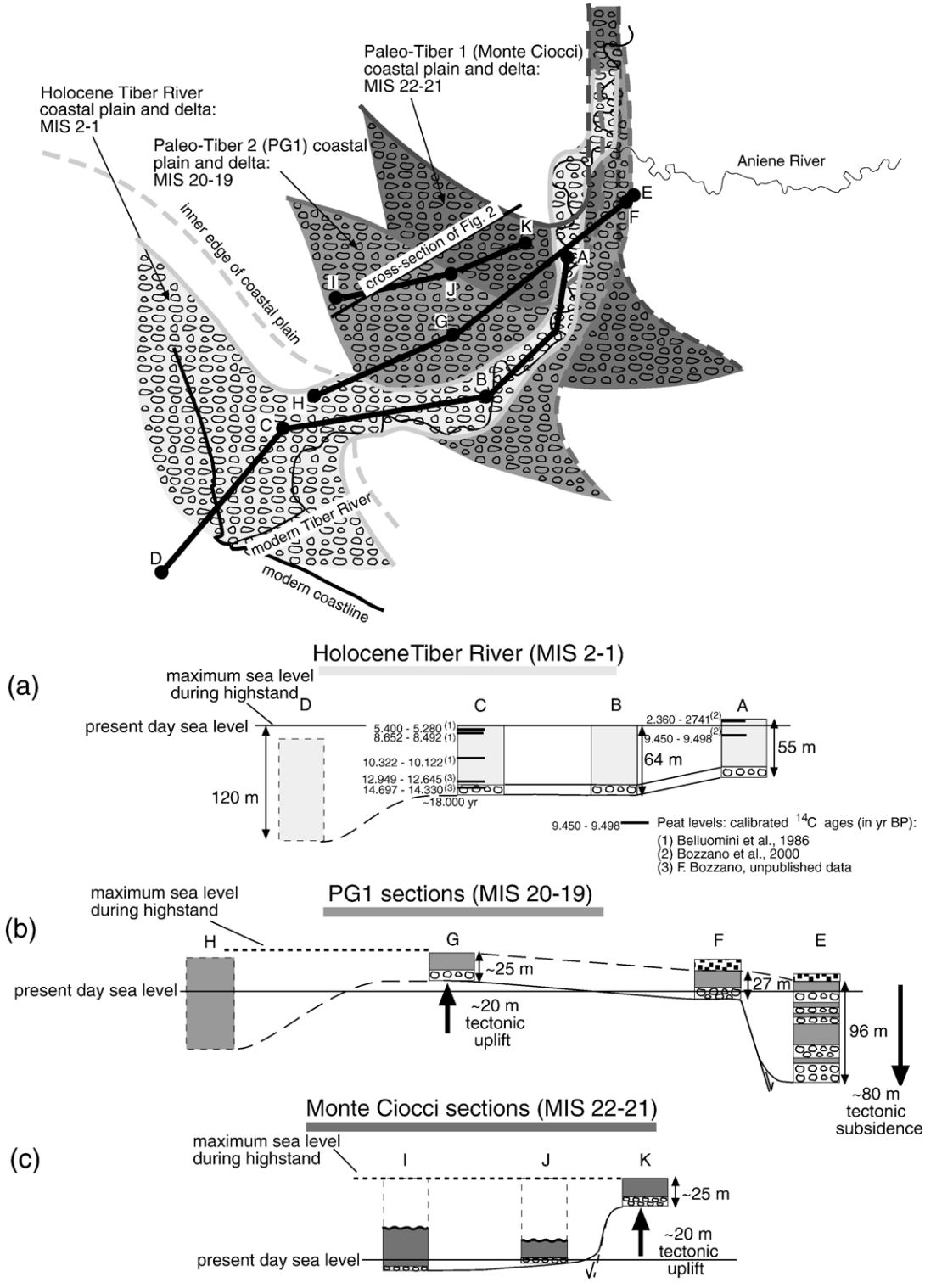

part of the core (from −5.0 to −11 m a.s.l.) indicate the presence of magnetite along with greigite.

5. Discussion

5.1. Stratigraphic interpretation

Our chronostratigraphic investigations indicate that two different aggradational sections, which correlate with MIS 19 and MIS 15, were deposited laterally from north to south and erosionally above the Plio-Pleistocene substrate in central to southern Rome. This differs from previous interpretations [5,6] in which a single basal aggradational section, correlated to MIS 17, was inferred to exist throughout this area. Recognition of these two different aggradational sections, hereby named the paleo-Tiber 2 and paleo-Tiber 4 sequences, is based on the $^{40}Ar/^{39}Ar$ ages of intercalated tephra layers and on the magnetic polarity zonation of the clay deposits of each sedimentary cycle, which enables us to correlate them to MIS 19 and MIS 15, respectively. These names are used in order to match with those of the MIS 21 and MIS 17 sections, which we now refer to as paleo-Tiber 1 and paleo-Tiber 3 sections, respectively. Below, we successively discuss the aggradational sections, combining new data from this study with previously published data, in order to explain the depositional history of the Tiber River delta.

5.1.1. MIS 21 = Paleo-Tiber 1 section (=Monte Ciocci Formation)

The geochronologic and stratigraphic evidence suggest that no section corresponding to MIS 21 exists beneath central Rome. It is probable that the only remnants of this oldest aggradational section are those found at about 55 m a.s.l. to the west of the Tiber River Valley (Monte Ciocci and Gianicolo Hill localities; Figs. 1 and 2).

5.1.2. MIS 19 = Paleo-Tiber 2 section (=Ponte Galeria Formation 1 (PG1))

Fig. 4b is an enlargement of the inset box in Fig. 3a, and is a summary of the stratigraphic, geochronologic and paleomagnetic data from borecores on which we base the correlation of the first (oldest) aggradational section in central Rome to Glacial Termination IX at the beginning of MIS 19. As discussed above, the tephra layers recovered from borecores PT-S2, PT-S6, PT-S14, I-7, and I-9 were deposited by at least two different eruptions dated at 803±8 ka and 783±10 ka, respectively. No tephra layers were found in the clay deposits in two of the borecores (VVM and PSA) on which paleomagnetic analysis was performed (Fig. 4b). However, stratigraphic correlation of the cores shown in Fig. 4b demonstrates that the clay horizon between the upper gravel layer and the sandy clay layer with carbonate concretions was deposited during the same chronostratigraphic event.

Based on radioisotopic and paleomagnetic data, we relate the deposition of the investigated clay section to the marine transgression associated with Glacial Termination IX, which, based on the insolation-tuned benthic $\delta^{18}O$ stack in Lisiecki and Raymo [10], occurred at 780 ka. Thus, the aggradational section of basal gravel and the overlying clay section in central-northern Rome correlate to MIS 19. This sequence must therefore be considered synchronous with the Ponte Galeria 1 formation in the Ponte Galeria area to the west (Basal Conglomerate and *Helicella* Clay, sensu Conato et al. [28]). Following this, we interpret the entire multi-layered gravel and clay succession that fills the paleo-Tiber graben to correlate with the single gravel horizon in the center of Rome and in Ponte Galeria. Thus, following Marra and Rosa [5], the paleo-Tiber graben fill is interpreted to have been influenced by syn-sedimentary tectonics (see Fig. 9b), rather than being the result of repeated episodes of channel and fill deposition.

5.1.3. MIS 17 = Paleo-Tiber 3 section (=Ponte Galeria Formation 2 (PG2))

The Ponte Galeria 1 formation in Ponte Galeria is followed by a second aggradational section, the Ponte Galeria 2 formation, which has been correlated to MIS 17 [3]. The Ponte Galeria 2 formation has a basal gravel and sand layer that was deposited in a littoral

Fig. 9. Paleogeography of the Tiber River delta, with distribution of the basal coarse-grained sediments of three different aggradational sections deposited during Glacial Terminations IX, VII and I. Remnants of the penultimate depositional cycle (MIS 5 Tyrrhenian Stage aggradational section) are also shown. Southwestward (seaward) shifting of the position of the Tiber delta from the oldest aggradational section (Monte Ciocci sequence; MIS 22-21) to the youngest one (Holocene section of the Tiber River) indicates progradation induced by tectonic uplift of the coastal area. Cross-section a): longitudinal profile of the Holocene sedimentary section of the Tiber River, reconstructed from borecore data (A, B, C, C′, C″); section D is an estimated thickness for the outer delta. Ages of intercalated peat levels indicate that aggradation was coeval throughout the fluvial system and that the transition from the coarse-(basal gravel) to fine-grained (clay) units was coincident with the last glacial termination (~13.8 ka, [32]). Cross-sections b) and c) are equivalent profiles for the first two aggradational sections of the paleo-Tiber River, with present elevation above sea level, stratigraphic features and tectonic interpretations indicated.

environment [3] and an upper layer of lagoonal to littoral clay ("sand and gravel with frequent cross-lamination" and "*Venerupis senescens* clay" of Conato et al. [28]). A volcaniclastic layer within the gravel at the base of the Ponte Galeria 2 aggradational section in Ponte Galeria yielded an $^{40}Ar/^{39}Ar$ age of 758±4 ka (age re-calculated by Karner et al. [11] from data in Marra et al. [3]), which allows correlation of the start of Ponte Galeria 2 deposition to the sea level lowstand of MIS 18. However, petrographic features of this volcaniclastic layer, including substantial mixing with clastic sediment, suggest significant reworking, and thus we interpret this age to be the maximum age estimation for Glacial Termination VIII (i.e. the termination cannot be older than 758±4 ka).

We suggest that the correlative inland portion of the Ponte Galeria 2 section in Rome is represented by the sandy clay deposit with carbonate concretions that unconformably overlies the grey clay of the paleo-Tiber 2 section. We therefore name it the paleo-Tiber 3 section. The absence of this deposit in southern Rome, where a younger aggradational section (correlated to MIS 15) is present (Fig. 3b), supports this interpretation. The sandy clay deposit with carbonate concretions was already interpreted as a distinct aggradational section (paleo-Tiber 2b unit) by Marra and Rosa [5] based on the unconformable contact with the lower gray clay and based on gravel locally at its base. However, the lack of geochronologic age constraint and having correlated the underlying aggradational section to MIS 17 caused them to interpret it as having been deposited during MIS 15.

5.1.4. MIS 15 = Paleo-Tiber 4 section (=Santa Cecilia Formation)

We interpret that a younger aggradational section is present in southern Rome (Fig. 3b) and correlate it to MIS 15, based on the $^{40}Ar/^{39}Ar$ age of 649±2 ka for a tephra layer in the INGV core from southern Rome (Table 1, Fig. 3b). The clay deposit recovered in the INGV borecore has normal magnetic polarity, in agreement with the radioisotopic age of the tephra at its base. We have tentatively located the northern margin of this younger aggradational section in the cross-section in Fig. 3b based on the lack of the sand with carbonate concretion unit in the southernmost boreholes.

Previous correlation of the first aggradational section in Rome to MIS 17 was based on paleomagnetic investigation of a borecore taken near the Colosseum [6] in which the clay has normal polarity (COL in Fig. 3b). The mineral responsible for the magnetic signal in the Colosseum core is magnetite; therefore it is unlikely that the magnetization is a later diagenetic remagnetization. Therefore, in Fig. 3b we attribute the sediments beneath the Colosseum to the paleo-Tiber 4 unit.

5.2. Paleoclimate implications

In order to discuss the paleoclimatic significance of the Tiber River aggradational sections, we need to establish the relationship between the timing of their deposition and sea level changes caused by glacial cycles. We begin by comparing Glacial Termination I with Holocene deposition in the Tiber River delta. In Fig. 9, we show the geographic distribution, lithostratigraphy and calibrated ^{14}C ages [29–31] of these deposits. The Holocene Tiber River sediments contain a single gravel horizon at the base of the aggradational section. The top of this horizon uniformly decreases in elevation throughout the fluvial channel and in the coastal plain (Fig. 9). The gravel grades upward to sand and clay. ^{14}C ages of peat within the alluvial deposit indicate that clay deposition began between 14,697–14,330 ka Cal BP and 12,949–12,645 ka Cal BP (F. Bozzano, unpublished data). These ^{14}C ages demonstrate that the gravel at the base of the aggradational section in the Tiber River channel and coastal plain was deposited primarily between the last glacial maximum (~19 ka [32]) and the glacial termination (~14 ka [33]). Thus, we interpret that the onset of deposition of the fine-grained portion of the aggradational section coincided with the last glacial termination, in response to sea-level rise. The lower portion of this fine-grained section was rapidly deposited, as indicated by ^{14}C ages (approximately 90% of the clay was deposited in this locality by 8.5 ka). This also indicates that sea level had risen to −7 m from its present elevation by 8.5 ka, in good agreement with coral records of sea level [31,33]. Other ^{14}C ages from borecores within Rome in a tributary of the Tiber River (the Velabrum [34]) more thoroughly document inland Holocene aggradation. Similar to data from the coastal plain and the main fluvial section, these data indicate that most of the aggradation occurred by about 8 ka, after which sedimentation significantly slowed.

Compared to the insolation-tuned $\delta^{18}O$ record of Lisiecki and Raymo [10], the ^{14}C dates of the gravel-clay transition from the Tiber River sedimentary record provide an excellent match with the timing of the last glacial termination at 14 ka (Fig. 10). In particular, no apparent lead or lag can be inferred between the time of the sedimentary switch and the occurrence of the glacial termination. Using this Holocene analog, ages of volcanic layers interbedded within older aggradational sections of the Tiber River can help to date past glacial

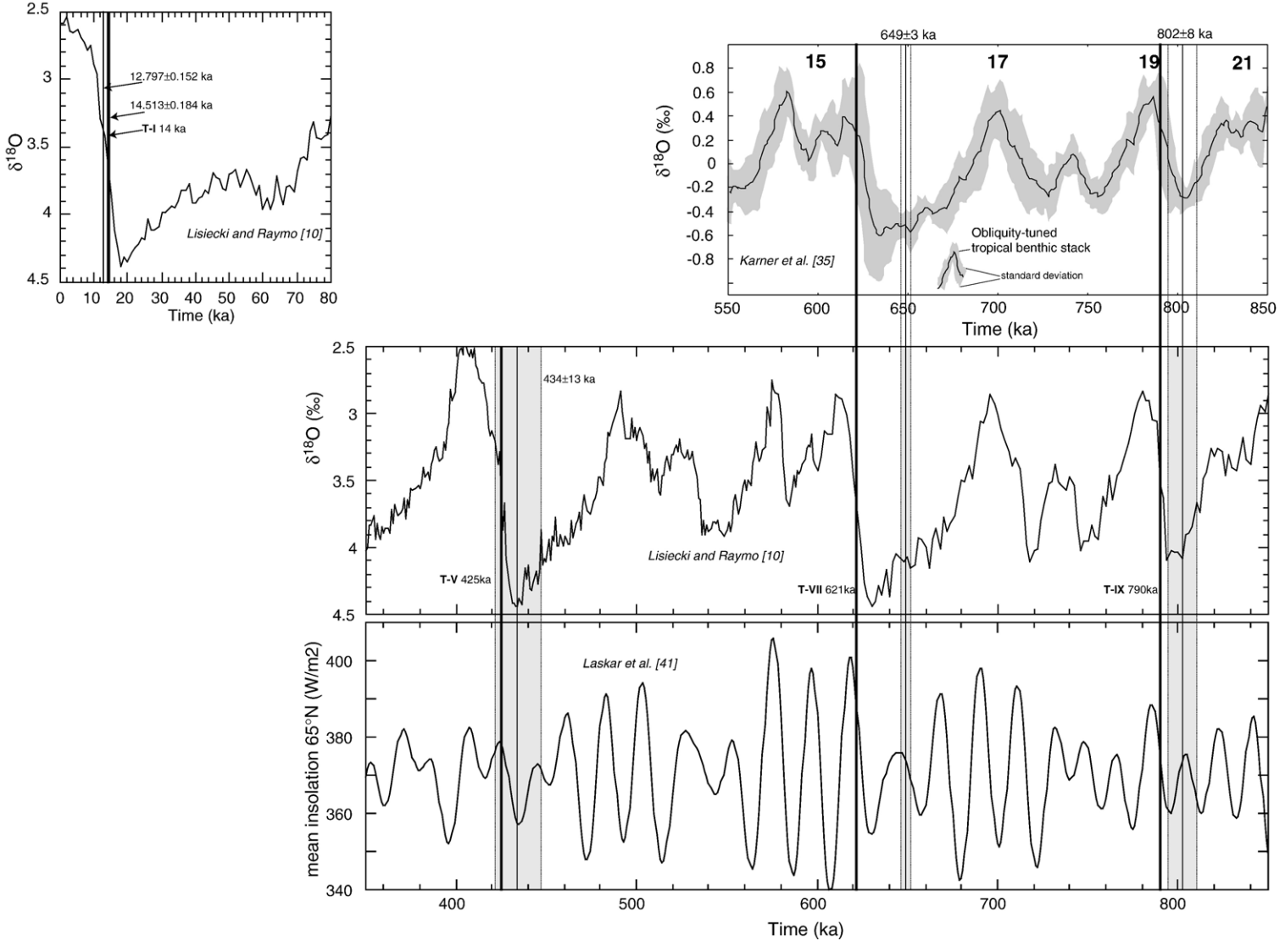

Fig. 10. Comparison of radioisotopic ages of Glacial Terminations IX and VII interpreted from the continental sedimentary record of the Tiber River (shadowed bars are the full (systematic plus analytical) age errors), with two orbitally-calibrated $\delta^{18}O$ time-scales: the astronomically tuned stack of Lisiecki and Raymo [10]; and the obliquity-tuned tropical benthic stack of Karner et al. [35]. Data for two younger terminations (Termination V [38] and I (this work) are also shown. Similar to the obliquity-tuned tropical benthic stack, the Tiber River delta ages for Glacial Terminations IX, VII and V appear to pre-date the timing of glacial terminations predicted by the astronomically tuned global $\delta^{18}O$ benthic stack. A comparison with the insolation curve at 65° N latitude [41] is also provided.

terminations. In particular, ages of tephra layers that occur at the transition from coarse- to fine-grained sedimentation can be interpreted to date the glacial termination. While other features of an aggradational section, such as thickness and depositional environment, may be influenced by the amplitude of the glacial signal and by local tectonic movements, the sharp transition from coarse- to fine-grained sedimentation in these sections appears to be unequivocally controlled by the significant change in baselevel at the glacial termination. Tectonic effects (i.e. regional subsidence) in the early stages of deglaciation may produce local transgression within the coastal plain and a temporary switch of sediments from gravel to clay (as is observed for the paleo-Tiber River at around 800 ka, as mentioned above). However, the ultimate change in the river system transport competence, which originates a clear bipartition in a lower coarse-sized portion and an upper fine-sized portion in the sedimentary succession, is a recurrent feature that characterizes all of the aggradational sections recognized in the paleo-Tiber River delta [1–3]. Age constraints previously provided for several of these aggradational sections strongly support the interpretation that the sedimentary switch from gravel to clay correspond to a sudden loss in sediment transport competence induced by change in the coastal dynamics (increased accommodation space, coastline retreat, change in sediment supply), associated with the glacial termination. We therefore assign the ages from tephra layers from the transition from coarse- to fine-grained portions of two different aggradational sections to Glacial Terminations IX and VII, respectively. These ages, considering the full errors (analytical and systematic errors), are as follows.

1) Glacial Termination IX: 802±8 ka (1σ). This age is from a primary tephra layer at the base of the finer-grained portion of the paleo-Tiber 2 section in borecore PT-S2, which is precisely at the transition from coarse-to fine-grained sedimentation.
2) Glacial Termination VII: 649±3 ka (1σ). This age is from a primary tephra layer at the top of the basal gravel horizon of the paleo-Tiber 4 section recovered in the INGV borecore. Again, the position of this tephra at the transition from coarse- to fine-grained sedimentation provides an excellent age for the timing of Termination VII.

When these ages are compared to those estimated in the benthic $\delta^{18}O$ stack tuned to June 65° N insolation of Lisiecki and Raymo [10] , it appears that the Tiber River ages pre-date the ages of glacial terminations predicted from such an astronomical calibration (Fig. 10). The disagreement with the insolation-estimated age of Glacial Termination IX is 6 kyr beyond the 2σ error we calculated for the tephra layer in borecore PT-S2. Whether this age for Termination IX is consistent with the orbitally-based chronology presented in Lisiecki and Raymo [10] depends on a complete error analysis of the benthic stack tuning process; such an analysis is beyond the scope of this paper. However, now that $^{40}Ar/^{39}Ar$ based chronologies have become sufficiently precise to test the accuracy of orbital tuning, it seems prudent for future orbital tuning work to include such error analysis (e.g. Karner et al. [35]).

The age of Glacial Termination VII (649±3 ka, 1σ full errors) interpreted from the paleo-Tiber sedimentary record appears to predate by 22 kyr (beyond the 2σ full errors) Termination VII in the orbitally-tuned benthic stack of Lisiecki and Raymo [10]. Based on the petrographic features of the dated volcanic layer interbedded in the sedimentary record, we exclude reworking of the pyroclastic-flow deposit.

A possible explanation that we have considered for this large mismatch may be regional tectonism at around 650 ka that lowered the paleo-Tiber delta area by several tens of meters. Tectonic subsidence on this order could produce a significant ingression, originating an early sedimentary switch in the coastal plain, where clay deposition starts several kiloyears before the climate signal and continues throughout the glacial termination. However, the similar elevation of the coast lines, as inferred from the high stand-systems tract deposits of MIS 17 and MIS 15 seems to exclude that large relative vertical movements occurred in the paleo-Tiber delta during this time interval [4].

Alternatively, similar to other terrestrial proxies of climate oscillations that also pre-date the astronomical ages for glacial terminations (e.g. [2,36,37]), the disagreement between our radioisotopically based record and orbitally-based timescales might be interpreted to suggest that the Milankovitch template of June 65° N insolation does not provide accurate ages for all glacial terminations. Previous constraints from tephra layers intercalated in the paleo-Tiber sedimentary sections [2,38] for Glacial Terminations III, V, and VI agree better with the ODP Site 806 obliquity-tuned timescale [39], than with the Site 806 record when it was tuned to the Milankovitch Template [40]. In the same way, the timing of Glacial Terminations IX and VII predicted from an obliquity-tuned tropical benthic stack [41] seems in better agreement (in the sense that it reduces the mismatch) with the ages from the paleo-Tiber sections than with the tuning of Lisiecki and Raymo [10] (Fig. 10). In Fig. 10,

we also compare the ages of Glacial Terminations V, VII, and IX interpreted from the sedimentary record of the paleo-Tiber River with insolation at 65°N [41]. Excluding a systematic external forcing (e.g. tectonics) on the older sedimentary record, the consistent misalignment of the timing of glacial terminations estimated from the aggradational sections of the paleo-Tiber with insolation maxima (one precession cycle in the case of Terminations IX and VII, while in the case of Termination V the larger associated error allows for a match with the astronomical tuning) may be suggestive either of:

i) a problem for the astronomical calibration of paleoclimate signals,
ii) an as-yet-unrealised systematic error associated with $^{40}Ar/^{39}Ar$ dating.

Since these possible sources of error are all testable, we believe that future studies will identify the probable source.

6. Conclusions

Aggradational sections of the Tiber River flood plain were deposited in response to glacio-eustatic sea level change at each glacial termination since the mid-Pleistocene climate transition. By means of stratigraphic data, paleomagnetic investigation, and $^{40}Ar/^{39}Ar$ ages of tephra layers, we have better identified and constrained the ages of two sedimentary sections that were deposited during MIS 20-19 and MIS 16-15 (~800-600 ka). Sedimentary features and ^{14}C geochronology from available literature for the modern Tiber River fluvial channel and alluvial plain deposits demonstrate that the sudden transition from a basal coarse-grained (gravel) to an upper fine-grained (clay) deposit is coincident with glacial terminations. Based on these data, we estimate the ages of Glacial Terminations IX and VII to be 802 ±8 ka (1σ full errors) and 649±3 ka (1σ full errors), respectively. These ages pre-date those predicted by astronomical tuning models that use a full-insolation (i.e. eccentricity, obliquity and precession) tuning target, but are in better agreement with alternative tuning of $\delta^{18}O$ records (e.g. obliquity-tuned time scales). Far from providing evidence for rejecting the Milankovitch's theory, these data should contribute to keep the discussion about calibration of the $\delta^{18}O$ curve alive.

Acknowledgments

We thank Enzo Boschi for supporting and encouraging our research, Leonardo Lombardi for suggestions and discussions concerning study of the paleo-Tiber underneath Rome, and Carlo Rosa for invaluable contributions to the stratigraphic study of boreholes and years of common field study. Reconstruction of the buried geology of Rome would had not been possible without the expert contributions of: Francesca Bozzano, Angelo Corazza, Vittorio Federici, Renato Funiciello, Maurizio Lanzini, Massimo Lenoci, Marcello Martinelli, Maurizio Martino, Pietro Nigro, Roberto Salucci, and Claudio Succhiarelli. We thank Richard Pearce for assistance with the SEM at the NOCS.DK thanks the Ann and Gordon Getty Foundation and the Folger Foundation for partial support of this work.

Appendix A. Supplementary data

Supplementary data associated with this article can be found, in the online version, at 10.1016/j.epsl.2007.01.014.

References

[1] D.B. Karner, P.R. Renne, $^{40}Ar/^{39}Ar$ geochronology of Roman province tephra in the Tiber River Valley: age calibration of Middle Pleistocene sea-level changes, Geol. Soc. Amer. Bull. 110 (1998) 740–747.
[2] D.B. Karner, F. Marra, Correlation of fluviodeltaic aggradational sections with glacial climate history: a revision of the classical Pleistocene stratigraphy of Rome, Geol. Soc. Amer. Bull. 110 (1998) 748–758.
[3] F. Marra, F. Florindo, D.B. Karner, Paleomagnetism and geochronology of early Middle Pleistocene depositional sequences near Rome: comparison with the deep sea $\delta^{18}O$ climate record, Earth Planet. Sci. Lett. 159 (1998) 147–164.
[4] D.B. Karner, F. Marra, F. Florindo, E. Boschi, Pulsed uplift estimated from terrace elevations in the coast of Rome: evidence for a new phase of volcanic activity? Earth Planet. Sci. Lett. 188 (2001) 135–148.
[5] F. Marra, C. Rosa, Stratigrafia e assetto geologico dell'area romana, in "La Geologia di Roma. Il Centro Storico", Mem. Descr. Carta Geol. Ital. 50 (1995) 49–118.
[6] F. Florindo, F. Marra, A revision for the Middle Pleistocene continental deposits of Rome (Central Italy): paleomagnetic data, Ann. Geofis. 38 (1995) 177–188.
[7] S. Milli, Depositional setting and high-frequency sequence stratigraphy of the middle-upper Pleistocene and Holocene deposits of the Roman basin, Geol. Rom. 33 (1997) 99–136.
[8] G. Giordano, A. Esposito, D. De Rita, M. Fabbri, I. Mazzini, A. Trigari, C. Rosa, R. Funiciello, The sedimentation along the Roman coast between middle and upper Pleistocene: the interplay of eustatism, tectonics and volcanism — new data and review, Quaternario 16 (2003) 121–129.
[9] F. Marra, M.G. Carboni, L. De Bella, C. Faccenna, R. Funiciello, C. Rosa, Il substrato Plio-Pleistocenico dell'area Romana, Boll. Soc. Geol. Ital. 114 (1995) 195–214.
[10] L.E. Lisiecki, M.E. Raymo, A Pliocene-Pleistocene stack of 57 globally distributed benthic $\delta^{18}O$ records, Paleocenography 20 (2005) PA 1003, doi:10.1029/2004PA001071.

[11] D.B. Karner, F. Marra, P. Renne, The history of the Monti Sabatini and Alban Hills volcanoes: groundwork for assessing volcanic–tectonic hazards for Rome, J. Volcanol. Geotherm. Res. 107 (2001) 185–219.
[12] P.R. Renne, C.C. Swisher, A.L. Deino, D.B. Karner, T.L. Owens, D.J. DePaolo, Intercalibration of standards, absolute ages and uncertainties in $^{40}Ar/^{39}Ar$ dating, Chem. Geol. 145 (1998) 117–152.
[13] N. Tetley, I. McDougall, H.R. Heydegger, Thermal neutron interferences in the $^{40}Ar/^{39}Ar$ dating technique, J. Geophys. Res. 85 (1980) 7201–7205.
[14] P.R. Renne, K. Deckart, M. Ernesto, G. Féraud, E.M. Piccirillo, Age of the Ponta Grossa dike swarm (Brazil) and implications for Paraná flood volcanism, Earth Planet. Sci. Lett. 144 (1996) 199–211.
[15] J.L. Kirschvink, The least-squares line and plane and the analysis of palaeomagnetic data, Geophys. J. R. Astron. Soc. 62 (1980) 699–718.
[16] A.P. Roberts, Magnetic characteristics of sedimentary greigite (Fe_3S_4), Earth Planet. Sci. Lett. 134 (1995) 227–236.
[17] M.J. Dekkers, Magnetic properties of natural pyrrhotite. II. High- and low-temperature behaviour of Jrs and TRM as function of grain size, Phys. Earth Planet. Inter. 57 (1989) 266–283.
[18] I.F. Snowball, Gyroremanent magnetization (GRM) and the magnetic properties of greigite bearing clays in southern Sweden, Geophys. J. Int. 129 (1997) 624–636.
[19] L. Sagnotti, A. Winkler, Rock magnetism and paleomagnetism of greigite-bearing mudstones in the Italian peninsula, Earth Planet. Sci. Lett. 165 (1999) 67–90.
[20] A.P. Roberts, C.R. Pike, K.L. Verosub, FORC diagrams: a new tool for characterizing the magnetic properties of natural samples, J. Geophys. Res. 105 (2000) 28,461–28,475.
[21] A.P. Roberts, Q.S. Liu, C.J. Rowan, L. Chang, C. Carvallo, J. Torrent, C.S. Horng, Characterization of hematite (α-Fe_2O_3), goethite (α-FeOOH), greigite (Fe_3S_4), and pyrrhotite (Fe_7S_8) using first-order reversal curve diagrams, J. Geophys. Res. 111 (2006) B12535, doi:10.1029/2006JB004715.
[22] R. Raiswell, Pyrite texture, isotopic composition and the availability of iron, Am. J. Sci. 282 (1982) 1244–1263.
[23] A.P. Roberts, R. Weaver, Multiple mechanisms of remagnetization involving sedimentary greigite (Fe_3S_4), Earth Planet. Sci. Lett. 231 (2005) 263–277.
[24] F. Florindo, L. Sagnotti, Paleomagnetism and rock magnetism in the upper Pliocene Valle Ricca (Rome, Italy) section, Geophys. J. Int. 123 (1995) 340–354.
[25] W.T. Jiang, C.S. Horng, A.P. Roberts, D.R. Peacor, Contradictory magnetic polarities in sediments and variable timing of neoformation of authigenic greigite, Earth Planet. Sci. Lett. 193 (2001) 1–12.
[26] H. Oda, M. Torii, Sea-level change and remagnetization of continental shelf sediments off New Jersey (ODP Leg 174A): magnetite and greigite diagenesis, Geophys. J. Int. 156 (2004) 443–458.
[27] C.J. Rowan, A.P. Roberts, Magnetite dissolution, diachronous greigite formation, and secondary magnetizations from pyrite oxidation: Unravelling complex magnetizations in Neogene marine sediments from New Zealand, Earth Planet. Sci. Lett. 241 (2006) 119–137.
[28] V. Conato, D. Esu, A. Malatesta, F. Zarlenga, New data on the Pleistocene of Rome, Quaternaria 22 (1980) 131–176.
[29] F. Bozzano, A. Andreucci, M. Gaeta, R. Salucci, A geological model of the buried Tiber River valley beneath the historical centre of Rome, Bull. Eng. Geol. Environ. 59 (2000) 1–21.
[30] G. Belluomini, P. Iuzzolini, L. Manfra, R. Mortari, M. Zalaffi, Evoluzione recente del delta del Tevere, Geol. Rom. 25 (1986) 213–234.
[31] K. Lambeck, F. Antonioli, A. Purcell, S. Silenzi, Sea-level change along the Italian coast for the past 10,000 yr, Quat. Sci. Rev. 23 (2004) 1567–1598.
[32] E. Bard, B. Hamelin, R. Fairbanks, U–Th ages obtained by mass spectrometry in corals from Barbados: sea level during the past 130,000 years, Nature 346 (1990) 456–458.
[33] E. Bard, B. Hamelin, M. Arnold, L. Montaggioni, G. Cabioch, G. Faure, F. Rougerie, Deglacial sea-level record from Tahiti corals and the timing of global meltwater discharge, Nature 382 (1996) 241–244.
[34] A.J. Ammerman, J. Miller, S. Ramsay, The mid-Holocene environment of the Velabrum in Rome, Soc. Preist. Protostor. Reg. Friuli-Venezia Giulia, Quad., Trieste 8 (2000) 9–20.
[35] D.B. Karner, J. Levine, B.P. Medeiros, R.A. Muller, Constructing a stacked benthic $\delta^{18}O$ record, Paleoceanography 17 (3) (2002), doi:10.1029/2001PA000667.
[36] I.J. Winograd, T.B. Coplen, J.M. Landwehr, A.C. Riggs, K.R. Ludwig, B.J. Szabo, P.T. Kolesar, K.M. Revesz, Continuous 500,000-year climate record from vein calcite in Devils Hole, Nevada, Science 258 (1992) 255–260.
[37] K.R. Ludwig, K.R. Simmons, B.J. Szabo, I.J. Winograd, J.M. Landwehr, A.C. Riggs, R.J. Hoffman, Mass-spectrometric ^{230}Th–^{234}U–^{238}U dating of the Devils Hole calcite vein, Science 258 (1992) 284–287.
[38] D.B. Karner, F. Marra, $^{40}Ar/^{39}Ar$ dating of Glacial Termination V and the duration of Marine Isotopic Stage 11, Earth's Climate and Orbital Eccentricity: The Marine Isotope Stage 11 Question, Geophysical Monograph, vol. 137, American Geophysical Union, Washington, D.C., 2003, pp. 61–66.
[39] W.H. Berger, T. Bickert, H. Schmidt, T. Wefer, Quaternary oxygen isotope record of pelagic foraminifers; Site 806, Ontong Java Plateau: Proc. ODP. Sci. Res. 130 (1992) 381–395.
[40] W.H. Berger, T. Bickert, G. Wefer, M.I. Yasuda, Brunhes–Matuyama boundary: 790 k.y. date consistent with ODP Leg 130 oxygen isotope records based on fit to Milankovitch template, Geophys. Res. Lett. 22 (1995) 1525–1528.
[41] J. Laskar, F. Joutel, F. Boudin, Orbital, precessional and insolation quantities for the Earth from −20 Myr to +10 Myr, Astron. Astrophys. 270 (1993) 522–533.